



UNIVERSITY OF LEEDS

This is a repository copy of *Longitudinal structure of Earth's magnetic field controlled by lower mantle heat flow*.

White Rose Research Online URL for this paper:

<https://eprints.whiterose.ac.uk/195052/>

Version: Accepted Version

Article:

Mound, JE orcid.org/0000-0002-1243-6915 and Davies, CJ orcid.org/0000-0002-1074-3815 (2023) Longitudinal structure of Earth's magnetic field controlled by lower mantle heat flow. Nature Geoscience. ISSN 1752-0894

<https://doi.org/10.1038/s41561-023-01148-9>

This is an author produced version of a paper published in Nature Geoscience. Uploaded in accordance with the publisher's self-archiving policy. This version of the article has been accepted for publication, after peer review (when applicable) and is subject to Springer Nature's AM terms of use (<https://www.springernature.com/gp/open-research/policies/accepted-manuscript-terms>), but is not the Version of Record and does not reflect post-acceptance improvements, or any corrections. The Version of Record is available online at: <https://doi.org/10.1038/s41561-023-01148-9>.

Reuse

Items deposited in White Rose Research Online are protected by copyright, with all rights reserved unless indicated otherwise. They may be downloaded and/or printed for private study, or other acts as permitted by national copyright laws. The publisher or other rights holders may allow further reproduction and re-use of the full text version. This is indicated by the licence information on the White Rose Research Online record for the item.

Takedown

If you consider content in White Rose Research Online to be in breach of UK law, please notify us by emailing eprints@whiterose.ac.uk including the URL of the record and the reason for the withdrawal request.



eprints@whiterose.ac.uk
<https://eprints.whiterose.ac.uk/>

1 Lower Mantle Heat Flow Controls the Longitudinal 2 Structure of Earth's Magnetic Field

3 Jonathan E. Mound,^{1,*} Christopher J. Davies,¹

¹School of Earth and Environment, University of Leeds, Leeds, UK, LS2 9JT

*To whom correspondence should be addressed; E-mail: j.e.mound@leeds.ac.uk.

4 **Thermal interactions between Earth's core and mantle provide the power that**
5 **maintains the geomagnetic field. However, the observational expression of**
6 **these interactions and their unique potential to link magnetic field behaviour**
7 **and deep Earth processes has remained uncertain for decades. Here we show**
8 **that recent global time-dependent magnetic field models spanning tens of thou-**
9 **sands of years combined with numerical simulations indicate how the mantle**
10 **controls core dynamics. Simulations of rapidly rotating turbulent dynamo ac-**
11 **tion with strong imposed lateral variations in CMB heat flow reproduce the**
12 **morphology and secular variation of Earth's modern field, and the inferred**
13 **large-scale flow structure at the top of the core. These simulations reveal**
14 **that the long-term detectable signature of thermal core-mantle interactions**
15 **are equatorial patches of reverse flux, rather than the high-latitude patches**
16 **suggested by less Earth-like simulations. Comparison of our simulations with**
17 **observation models also suggest that the amplitude of the present-day hemi-**
18 **spheric imbalance in secular variation is anomalously large.**

19 **Introduction**

20 Earth’s global magnetic field has persisted throughout the majority of its history, generated
21 by a dynamo process in the liquid core that derives its power from the slow loss of heat to
22 the mantle (1). Convection within the mantle is characterised by much longer timescales and
23 much longer wavelengths than core convection and lateral variations in the temperature distri-
24 bution of the lowermost mantle result in a heterogeneous pattern of heat flow at the core-mantle
25 boundary (CMB), with enhanced/suppressed heat flux where the lowermost mantle is anoma-
26 lous cold/hot (2, 3). Yet the extent to which mantle heat flow controls the geodynamo and
27 geomagnetic field has been debated for decades. Variations in reversal frequency (4), apparent
28 preferred longitudes of transitional virtual geomagnetic poles (5), and persistently weak field
29 changes in the Pacific (6), all argued to result from the mantle’s influence on core dynamics,
30 have been disputed by both observational and modelling studies (7). However, recently a major
31 observational limitation—the lack of continuous global time-dependent representations of the
32 field covering more than a few core turnover times—has been addressed by new models, such
33 as GGF100k, covering the last 100 kyrs (8). By combining these models with numerical sim-
34 ulations of core dynamics we find that it is now possible to identify the magnetic signature of
35 thermal core-mantle interaction and its links to core dynamics.

36 A prominent feature of the geomagnetic field in high-resolution models covering the last
37 400 years (9) are the four high-latitude flux patches that appear at longitudes where mantle heat
38 flow is expected to be anomalous high. Convergent downwelling resulting from the locally el-
39 evated heat flow could cause intense flux patches to persistently concentrate around preferred
40 longitudes (7). However, while similar patches must be represented in realistic simulations of
41 core dynamics, observational models that precede the past four centuries (10) find that they
42 are not stationary, indicating that they could be transient features. Nevertheless, observational

43 studies agree that long-wavelength structure of Earth's time-averaged magnetic field contains
44 substantial non-zonal structure (10). Free convection in the core may give rise to magnetic
45 field structures with lifetimes comparable to the advective time scale (a few centuries); how-
46 ever, since mantle structure persists over geologically long times its influence should appear in
47 sufficiently long-term averages of Earth's magnetic field.

48 Another feature of the recent magnetic field is the preference for stronger secular variation
49 (SV) in the Atlantic hemisphere (11), a signature that has persisted for at least a few centuries
50 (9). Paleomagnetic reconstructions of Earth's magnetic field do not recover instantaneous SV;
51 however, they can provide measures of field variability throughout their duration. For example,
52 the paleosecular variation index (P_i) (12) is a non-dimensional measure of the paleo-field's
53 deviation from the expected dipole strength and structure at a given location (see Methods), and
54 temporal evolution of P_i provides insight into patterns of field variation over the last 100 kyr
55 (10). Although periods of enhanced activity in the Atlantic hemisphere are seen in long-term
56 records, so too are periods of enhanced Pacific activity (13–16); as with the structure of the field
57 itself, successful simulations must contain non-zonal SV features that are relatively long-lived
58 but not strictly stationary.

59 Secular variation arises from the interaction of the magnetic field and fluid flow at the top
60 of the outer core. Models derived from the inversion of secular variation data can thus provide
61 insight into core flow, although the details of the recovered flow depend on the treatment of
62 the data and the assumptions used to break the inherent non-uniqueness of the inversion (17).
63 Nevertheless, some features are consistently seen in these observationally derived models such
64 as relatively strong westward flow beneath the equatorial Atlantic, whereas flow beneath the
65 equatorial Pacific is generally weak or eastward (17–20). The large-scale flow is often charac-
66 terised as an equatorially symmetric eccentric gyre, with the westward Atlantic flow deviating
67 towards the poles near American longitudes, bypassing the Pacific at high latitudes, and return-

68 ing towards the equator by Indian longitudes (19, 21, 22).

69 Many previous studies have obtained simulated fields that are morphologically similar to the
70 present geomagnetic field (23–25); however, only one has also reported a match to the pattern
71 of modern SV (26). This result was obtained by adding two features to the standard geodynamo
72 model setup: gravitational coupling between the inner core and mantle, and a hemispheric pat-
73 tern of inner core growth due to convective translation. Although the strength of gravitational
74 coupling is relatively well constrained (27), recent determinations of core material properties
75 suggest that purely thermal convection of the inner core is highly unlikely and that purely com-
76 positional or doubly-diffusive thermochemical convection were more likely before the inner
77 core grew to half its present size (28–31). Here we instead seek solutions that match the field
78 and SV morphology based on a single well-established mechanism: lateral variations in heat
79 flow at the CMB.

80 **Results**

81 Our previous work has systematically investigated the effects of different patterns and ampli-
82 tudes of outer boundary forcing on bottom-driven non-magnetic rotating convection in spherical
83 shell geometry (32–34), a configuration that provides a simple analogue for core dynamics. Us-
84 ing knowledge of the regime diagram for homogeneous convection in the same setup (35) has
85 allowed us to run a targeted suite of dynamo simulations in the rapidly rotating and turbu-
86 lent dynamical regime that is thought to characterise Earth’s core. We therefore consider six
87 simulations (see Methods) with Ekman number $E = 10^{-5}$, and two values of the Rayleigh
88 number $Ra = \{2000, 6000\}$. The magnetic Prandtl number $Pm = 1$ is set to achieve a
89 Quasi-Geostrophic and Magnetic-Archimedian-Coriolis (QG-MAC) force balance and a mag-
90 netic Reynolds number $Rm \sim 1000$, as is expected in the core (1, 36, 37). Two simula-
91 tions employ homogeneous boundary conditions while four impose a pattern of CMB heat

92 flux heterogeneity derived from mantle seismic tomography (38) with amplitude described by
93 $q^* = (q_{\max} - q_{\min})/q_{\text{ave}} = \{2.3, 5.0\}$ (where, q_{\max} , q_{\min} , q_{ave} are the maximum, minimum, and
94 average values of CMB heat flux, respectively; see Methods). The models have been run for
95 10's of thousands of simulation years, sufficient time to resolve the long-term time-averaged
96 behaviour of the non-zonal field (25). Performing such simulations in the rapidly rotating pa-
97 rameter regime is computationally expensive, the six runs presented here requiring a total of
98 14.6 million cpu hours.

99 The GGF100k reconstruction (8) resolves only the longest wavelength features of Earth's
100 field and thus we begin by considering the time-averaged field of our simulations truncated to
101 spherical harmonic degree and order 4 (Figure 1, supplemental figure 1). The time-averaged
102 field of our $Ra = 2000$, $q^* = 0$ run lacks the non-zonal structure evident for Earth (e.g.,
103 figure 11 of (10), supplemental figure 1a). Our $Ra = 6000$, $q^* = 0$ run is a multipolar reversing
104 case and thus does not have a meaningful time-averaged field. Heterogeneous mantle forcing in
105 our $q^* \neq 0$ runs organises the flow near the top of the core, introducing non-zonal structure into
106 the time-averaged magnetic field, although the precise strength and location of this non-zonal
107 structure varies between our $q^* \neq 0$ simulations. Nevertheless, the non-zonal structure observed
108 in GGF100k (such as low radial flux under South America, which is also seen in our $q^* \neq 0$
109 simulations) is clearly far greater than that of our homogeneous model once it has been averaged
110 over many advection times. This suggests that some factor other than the internal dynamics of
111 the fluid core is responsible for the long-term non-zonal features of the field.

112 The spatial and temporal structure of the modern field (e.g., the last 400 years as described
113 in *gufm1*) are better resolved than its long-term behaviour, and we now investigate whether the
114 $q^* \neq 0$ simulations can match the geometry and secular variation of the modern field. We
115 evaluate the temporal evolution of geometric features of the radial CMB magnetic field in our
116 simulations with a set of widely-employed compliance criteria (24) (see Methods). While the

117 choice of criteria is subjective and these measures do not assess all observable properties of the
118 dynamo behaviour (24, 25), they are straightforward to compute given a spherical harmonic rep-
119 resentation of the magnetic field and are useful for suggesting periods of simulation behaviour
120 that are suitable for more detailed analysis. The measures of field structure from 400-year win-
121 dows of the simulations are compared to the values obtained from analysis of *gufm1* (9) to
122 provide a χ^2 measure of agreement between simulations and Earth's modern geomagnetic field.
123 These criteria are complemented by a measure of hemispheric imbalance in SV (H_{sv}) and its
124 variation which provides a χ^2 measure of compliance with respect to the quiet Pacific secu-
125 lar variation (16). With the exception of the non-dipole-dominated solution with $Ra = 6000$
126 and $q^* = 0$ all simulations produce periods of good or excellent agreement with the modern
127 geomagnetic field (supplemental figure 2). The $Ra = 2000$, $q^* = 5.0$ simulation is usually non-
128 compliant with the modern field, unlike the other three $q^* \neq 0$ simulations. All simulations also
129 have 400-year windows characterised by quiet Pacific SV, although the hemispheric imbalance
130 is generally less than that derived from *gufm1*.

131 Figure 2 compares the magnetic field and SV of the 400-year window from the $Ra = 2000$,
132 $q^* = 2.3$ simulation with the lowest χ^2 totals across all five measures to the structure of field and
133 secular variation in *gufm1*. This window occurred at approximately 25,700 model years and, as
134 expected from the low χ^2 value, reproduces many characteristics of Earth's modern geomag-
135 netic field, such as patches of intense flux at high latitude and quiet SV in the central Pacific.
136 The pattern of flow from this 400-year window has more structure than the time-averaged flow
137 of the full run (figure 2c,f) although certain features arising from the CMB heterogeneity, such
138 as the promotion of downwelling between approximately 30° – 50° west can be seen in both.

139 Including boundary heterogeneity alters the time-averaged structure of the magnetic and
140 velocity fields near the top of the core introducing persistent longitudinal structure. The hetero-
141 geneous boundary forcing drives flow that, in the time average, produces a large equatorially

142 symmetric gyre with westward flow at mid-to-low latitudes under Africa and the Atlantic (fig-
143 ure 2c). The flow from the gyre diverts poleward at American longitudes thereby avoiding the
144 Pacific, which is characterised by weak time-averaged flows when $q^* = 2.3$. The hemispheric
145 difference in the time-averaged flows near the surface of the core in the cases with $q^* \neq 0$ might
146 be expected to result in persistent longitudinal differences in the hemispheric balance of secu-
147 lar variation. However, there is no evidence for a preferred hemisphere of secular variation in
148 our simulations (supplemental table 2) and, therefore, on average they provide a fairly poor fit
149 (supplemental table 1) to the quiet Pacific secular variation associated with the historic geomag-
150 netic field. Direct measurement of secular variation requires continuous observation of Earth's
151 magnetic field, possible only in the modern era. However, the cumulative effect of SV can be es-
152 timated from time-dependent field models constructed from paleomagnetic and archeomagnetic
153 samples (13–15). These models are necessarily smoothed due to the unavoidable limitations in
154 the spatial and temporal sampling of the data, but they do not indicate that there is hemispheric
155 structure in geomagnetic variability on thousand-year time scales (16).

156 The longitudinal structure of the paleosecular variation index, P_i , provides another view on
157 the hemispheric balance of temporal activity, one that can be compared directly with observa-
158 tional models such as GGF100k. The variability of P_i is lower in our $Ra = 2000$, $q^* = 2.3$
159 simulation than in GGF100k (Figure 3); however, the simulation and observational models have
160 similar median values. Both the simulated and observed fields have times of P_i being high in
161 the Atlantic hemisphere and low in the Pacific hemisphere, but they also have times with the
162 opposite imbalance. Maps of mean P_i value (supplemental figure 4) show regional differences
163 in paleosecular activity in both the simulations and observations. P_i tends to be larger at higher
164 latitudes in our simulations and somewhat low over the equatorial Pacific in our $q^* \neq 0$ cases.
165 However, there are not large differences between P_i distributions at different longitudes in either
166 GGF100k or our simulations. For example, the median longitudinal P_i values in GGF100k and

167 the three $q^* \neq 0$ simulations that match modern field structure and SV never differ significantly
168 from 0.06, the mean value obtained from temporally and spatially averaging *gufm1*.

169 Times when the $Ra = 2000$, $q^* = 2.3$ simulation exhibits poor compliance relative to
170 *gufm1* primarily arise due to the emergence of very strong flux patches in certain high-latitude
171 locations, a signature which can be seen in the total time-averaged field of the simulation (Fig-
172 ure 1b). Although emphasis has previously been placed on the persistence of strong high-
173 latitude flux patches (39–41), the time-averaged fields of the heterogeneous cases also have
174 non-zonal structure at equatorial latitudes that is absent from the homogeneous case (figure 4).
175 Both $Ra = 2000$, $q^* \neq 0$ cases have a pair of reverse flux patches straddling the equator roughly
176 beneath South America, with a similar structure on the CMB beneath the Indian Ocean. As is
177 the case for the high-latitude patches, the detailed strength, structure, and location of these low-
178 latitude features varies with Ra and q^* but they are present in all of our $q^* \neq 0$ cases (see also
179 supplemental figure 3).

180 Discussion

181 We find that dynamo simulations with strong lateral CMB heat flux variations successfully
182 reproduce the main features of the large-scale field morphology and paleosecular activity de-
183 scribed in observation models of the modern field and the GGF100k model spanning the last
184 100 kyrs. Unlike other studies (42) our simulations were not tuned to produce Earth-like fields;
185 the control parameters were chosen to sit within the appropriate dynamic regime for Earth’s
186 core and a CMB heat flux heterogeneity pattern derived from seismic tomography imposed.
187 The bulk dynamics of our simulations obeys a QG-MAC balance, and previous work (36, 43)
188 has shown that this balance is maintained in simulations sampling a uni-dimensional path in
189 parameter space that leads towards parameters more similar to Earth’s core. The large-scale
190 dynamics at the top of the core in our simulations do not depend on inertial or viscous ef-

191 facts (44), which both become weaker as core conditions are approached. Previous work has
192 also found that small-scale free convection in the core’s interior does not disrupt large-scale
193 boundary-forced patterns (34, 36, 43). Therefore, we have reason to believe that the behaviour
194 we observe is robust. The detailed time-dependent dynamics, and hence the compliance with
195 Earth’s field, do vary between our $q^* \neq 0$ cases; however, they have similar large scale features
196 of mantle-induced flow and structure in the outermost core, and all produce instances where
197 both field and SV morphology comply with geomagnetic observations. Both the CMB heat flux
198 heterogeneity imposed by the mantle and the internal core dynamics affect the compliance of
199 the resultant geodynamo. A more extensive suite of simulations could determine what balance
200 of these factors is required for Earth-like behaviour; however, the fact that three of the four
201 heterogeneous cases have long stretches of time with good or excellent compliance suggest that
202 these results do not depend on a delicate balance of conditions.

203 Earlier studies, at higher Ekman number, tended to find that the dynamo would fail in sim-
204 ulations with large heterogeneous boundary forcing (23, 45). However, as in (46), we find that
205 our simulations maintain a dynamo despite peak-to-peak variations in heat flux being larger
206 than the average. Indeed, for the $Ra = 6000$ cases the inclusion of boundary heterogeneity acts
207 to stabilise the dynamo, as the homogeneously forced case was in a multi-polar reversing state.
208 As in previous work (23, 40, 41, 45, 46), the boundary heterogeneity organises flow near the top
209 of the core, in our simulations this results in the large-scale time-average flow forming an ec-
210 centric gyre (22, 47) without recourse to variations in lower mantle electrical conductivity (48)
211 or inner core translation (16, 26).

212 Early heterogeneously forced simulations often favoured the formation of four quasi-stationary
213 high latitude flux patches, with equatorial symmetric pairs at American and Siberian longi-
214 tudes (40). However, the relative strength and stability of these pairs varied with model param-
215 eters, such that a hemispheric imbalance in the time averaged field structure may arise (40, 46).

216 In our simulations, which similarly use a pattern derived from mantle tomography (38), strong
217 heterogeneous boundary forcing tends to promote one pair of high latitude flux patches near the
218 dateline (180° longitude), with the patch southeast of New Zealand generally the stronger of
219 the two. Core-mantle boundary heterogeneity may impart longitudinal structure into the long
220 term average of Earth's magnetic field, but the combination of our results and previous work
221 indicates that the location of that structure need not be a simple reflection of mantle thermal
222 structure as it also depends on the balance of forces within the core.

223 We also find that mantle influence on the core results in persistent non-zonal structure at
224 low latitudes. In studies at higher E and with Ra that is only slightly supercritical (23, 40) the
225 wavelength of convective rolls in the fluid core was much larger than in our simulations. In
226 those studies, the long-wavelength mantle pattern could couple to the large scale core flow and
227 produce a locked dynamo state with nearly steady flows spanning the fluid shell. The difference
228 between the scales of free convection and mantle forcing in our simulations mean that a locked
229 dynamo does not emerge. However, enhanced short-wavelength convective activity does occur
230 at low latitudes between the LLVPs, where the seismic model predicts relatively cool mantle
231 material and hence high CMB heat flux that promotes downwelling at the top of the core. This
232 results in the time-averaged magnetic fields of our $q^* \neq 0$ simulations tending to have pairs of
233 equator-straddling reverse flux patches beneath South America and the Indian Ocean (figure 4).
234 Because of the temporal variability of the flow and field in our simulations the prevalence of
235 reverse flux patches in these locations is not necessarily obvious in shorter time averages (e.g.,
236 the 400-year window of figure 2b) and thus may be more observable in paleomagnetic data than
237 in the modern field.

238 The Pacific and African LLVPs are taken to be anomalously hot in our model and thus tend
239 to suppress convection in the outermost core underneath them, particularly when $q^* = 5$. The
240 seismic velocity anomalies, and hence our inferred CMB heat flux anomalies, differ between

241 the two LLVPs, with stronger anomalies in the Pacific. Their geometries also differ, with the
242 Pacific LLVP elongated longitudinally, whereas the African LLVP is elongated latitudinally. In
243 our simulations small scale convective velocities, and hence short-wavelength variations of B_r ,
244 tend to be weaker beneath the anomalously hot LLVPs, which could result in weaker observed
245 secular variation. The difference in LLVP geometry and amplitude between the Pacific and
246 African hemispheres might then provide a mechanism for explaining why secular variation of
247 the modern geomagnetic field in the Pacific has been anomalously quiet (49).

248 Regional patterns of field structure and (paleo)secular variation differ somewhat between
249 our simulations and it is not computationally feasible to explore a wide range of patterns and
250 amplitudes of CMB heat flux heterogeneity. The consequences of uneven spatial and temporal
251 sampling and smoothing in paleomagnetic field models (10) also limits our ability to resolve
252 fine details of the structure and dynamics of Earth’s field prior to the modern observational
253 era. Nevertheless, we find that there is no statistically significant preference for a hemispheric
254 difference in secular variation in our $q^* \neq 0$ simulations, Holocene field models (16), or the pa-
255 leosecular activity index of GGF100k. This suggests that, although there is long-term non-zonal
256 structure in Earth’s magnetic field, the hemispheric imbalance in secular variation observed for
257 recent times is anomalously large. However, persistent features of the flow and field that arise
258 from the mantle control, such as the eccentric gyre and low-latitude reverse flux patches, should
259 be expected in the geological past for as long as the current distribution of LLVPs has been
260 present.

261 **Acknowledgments**

262 The authors thank Cathy Constable for useful discussion as well as Nathanaël Schaeffer and
263 two anonymous reviewers for constructive comments that improved this work. C.J.D. ac-
264 knowledges a Natural Environment Research Council Pushing the Frontiers award, reference

265 NE/V010867/1. Figures were produced using Matplotlib (50) and Cartopy (51).

266 **References**

- 267 1. M. Landeau, A. Fournier, H.-C. Nataf, D. Cébron, N. Schaeffer, *Nature Reviews Earth &*
268 *Environment* **3**, 255 (2022).
- 269 2. T. Nakagawa, P. J. Tackley, *Earth and Planetary Science Letters* **271**, 348 (2008).
- 270 3. S. Stackhouse, L. Stixrude, B. B. Karki, *Earth and Planetary Science Letters* **427**, 11
271 (2015).
- 272 4. P. Olson, R. Coe, P. Driscoll, G. Glatzmaier, P. Roberts, *Physics of the Earth and Planetary*
273 *Interiors* **180**, 66 (2010).
- 274 5. C. Laj, A. Mazaud, R. Weeks, M. Fuller, E. Herrero-Bervera, *Nature* **351**, 447 (1991).
- 275 6. R. R. Doell, A. Cox, *Science* **171**, 248 (1971).
- 276 7. D. Gubbins, *Earth's Core: Dynamics, Structure, Rotation*, V. Dehant, K. Creager, S.-I.
277 Karato, S. Zatman, eds., Geodynamics Series (2003), pp. 163–179.
- 278 8. S. Panovska, C. G. Constable, M. Korte, *Geochemistry Geophysics Geosystems* **19**, 4757
279 (2018).
- 280 9. A. Jackson, A. R. T. Jonkers, M. R. Walker, *Philosophical Transactions of the Royal Society*
281 *A: Mathematical, Physical and Engineering Sciences* **358**, 957 (2000).
- 282 10. S. Panovska, M. Korte, C. G. Constable, *Reviews of Geophysics* **57**, 1289 (2019).
- 283 11. C. C. Finlay, *et al.*, *Earth, Planets and Space* **72**, 156 (2020).

- 284 12. S. Panovska, C. G. Constable, *Geochemistry Geophysics Geosystems* **67**, 83 (2017).
- 285 13. M. Korte, C. Constable, *Physics of the Earth and Planetary Interiors* **188**, 247 (2011).
- 286 14. M. Korte, C. Constable, F. Donadini, R. Holme, *Earth and Planetary Science Letters* **312**,
287 497 (2011).
- 288 15. A. Nilsson, R. Holme, M. Korte, N. Suttie, M. Hill, *Geophysical Journal International* **198**,
289 229 (2014).
- 290 16. J. Mound, C. Davies, L. Silva, *Earth and Planetary Science Letters* **424**, 148 (2015).
- 291 17. R. Holme, *Core Dynamics* (Elsevier, 2015), pp. 91 – 113.
- 292 18. A. Jackson, J. Bloxham, D. Gubbins, *Dynamics of Earths Deep Interior and Earth Rota-*
293 *tion: Geophysical Monograph , IUGG Volume* pp. 97 – 107 (1993).
- 294 19. O. Barrois, M. D. Hammer, C. C. Finlay, Y. Martin, N. Gillet, *Geophysical Journal Inter-*
295 *national* **215**, 695 (2018).
- 296 20. K. A. Whaler, M. D. Hammer, C. C. Finlay, N. Olsen, *Geophysical Research Letters* **49**
297 (2022).
- 298 21. M. A. Pais, D. Jault, *Geophysical Journal International* **173**, 421 (2008).
- 299 22. N. Gillet, D. Jault, C. C. Finlay, *Journal of Geophysical Research: Solid Earth* **120**, 3991
300 (2015).
- 301 23. A. P. Willis, B. Sreenivasan, D. Gubbins, *Physics of the Earth and Planetary Interiors* **165**,
302 83 (2007).
- 303 24. U. R. Christensen, J. Aubert, G. Hulot, *Earth and Planetary Science Letters* **296**, 487
304 (2010).

- 305 25. C. J. Davies, C. G. Constable, *Earth and Planetary Science Letters* **404**, 238 (2014).
- 306 26. J. Aubert, C. C. Finlay, A. Fournier, *Nature* **502**, 219 (2013).
- 307 27. C. J. Davies, D. R. Stegman, M. Dumberry, *Geophysical Research Letters* **41**, 3786 (2014).
- 308 28. M. Pozzo, C. Davies, D. Gubbins, D. Alfè, *Earth and Planetary Science Letters* **393**, 159
309 (2014).
- 310 29. S. Labrosse, *Comptes Rendus Geoscience* **346**, 119 (2014).
- 311 30. K. H. Lythgoe, J. F. Rudge, J. A. Neufeld, A. Deuss, *Geophysical Journal International*
312 **201**, 764 (2015).
- 313 31. R. Deguen, T. Alboussière, S. Labrosse, *Geophysical Journal International* **214**, 88 (2018).
- 314 32. J. E. Mound, C. J. Davies, *Journal of Fluid Mechanics* **828**, 601 (2017).
- 315 33. J. Mound, C. Davies, S. Rost, J. Aurnou, *Nature Geoscience* **12**, 575 (2019).
- 316 34. J. E. Mound, C. J. Davies, *Geophysical Research Letters* **47**, e2020GL087715 (2020).
- 317 35. R. S. Long, J. E. Mound, C. J. Davies, S. M. Tobias, *Journal of Fluid Mechanics* **889**
318 (2020).
- 319 36. J. Aubert, T. Gastine, A. Fournier, *Journal of Fluid Mechanics* **813**, 558 (2017).
- 320 37. N. Schaeffer, D. Jault, H. C. Nataf, A. Fournier, *Geophysical Journal International* **211**, 1
321 (2017).
- 322 38. G. Masters, S. Johnson, G. Laske, H. Bolton, *Philosophical Transactions of the Royal*
323 *Society A: Mathematical, Physical and Engineering Sciences* **354**, 1385 (1996).
- 324 39. D. Gubbins, P. Kelly, *Nature* **365**, 829 (1993).

- 325 40. D. Gubbins, A. P. Willis, B. Sreenivasan, *Physics of the Earth and Planetary Interiors* **162**,
326 256 (2007).
- 327 41. P. Olson, M. Landeau, E. Reynolds, *Physics of the Earth and Planetary Interiors* **271**, 1
328 (2017).
- 329 42. D. G. Meduri, *et al.*, *Geophysical Research Letters* **48** (2021).
- 330 43. J. Aubert, *Geophysical Journal International* **219**, S137 (2019).
- 331 44. C. J. Davies, J. E. Mound, *Geophysical Journal International* **219**, S21 (2019).
- 332 45. P. Olson, U. R. Christensen, *Geophysical Journal International* **151**, 809 (2002).
- 333 46. S. Sahoo, B. Sreenivasan, *Earth and Planetary Science Letters* **549**, 116507 (2020).
- 334 47. C. C. Finlay, A. Jackson, N. Gillet, N. Olsen, *Geophysical Journal International* **189**, 761
335 (2012).
- 336 48. M. Dumberry, C. More, *Nature Geoscience* **13**, 516 (2020).
- 337 49. R. Holme, N. Olsen, F. L. Bairstow, *Geophysical Journal International* **186**, 521 (2011).
- 338 50. J. D. Hunter, *Computing in Science and Engineering* **9**, 90 (2007).
- 339 51. Met Office, *Cartopy: a cartographic python library with a matplotlib interface*, Exeter,
340 Devon (2010 - 2015).

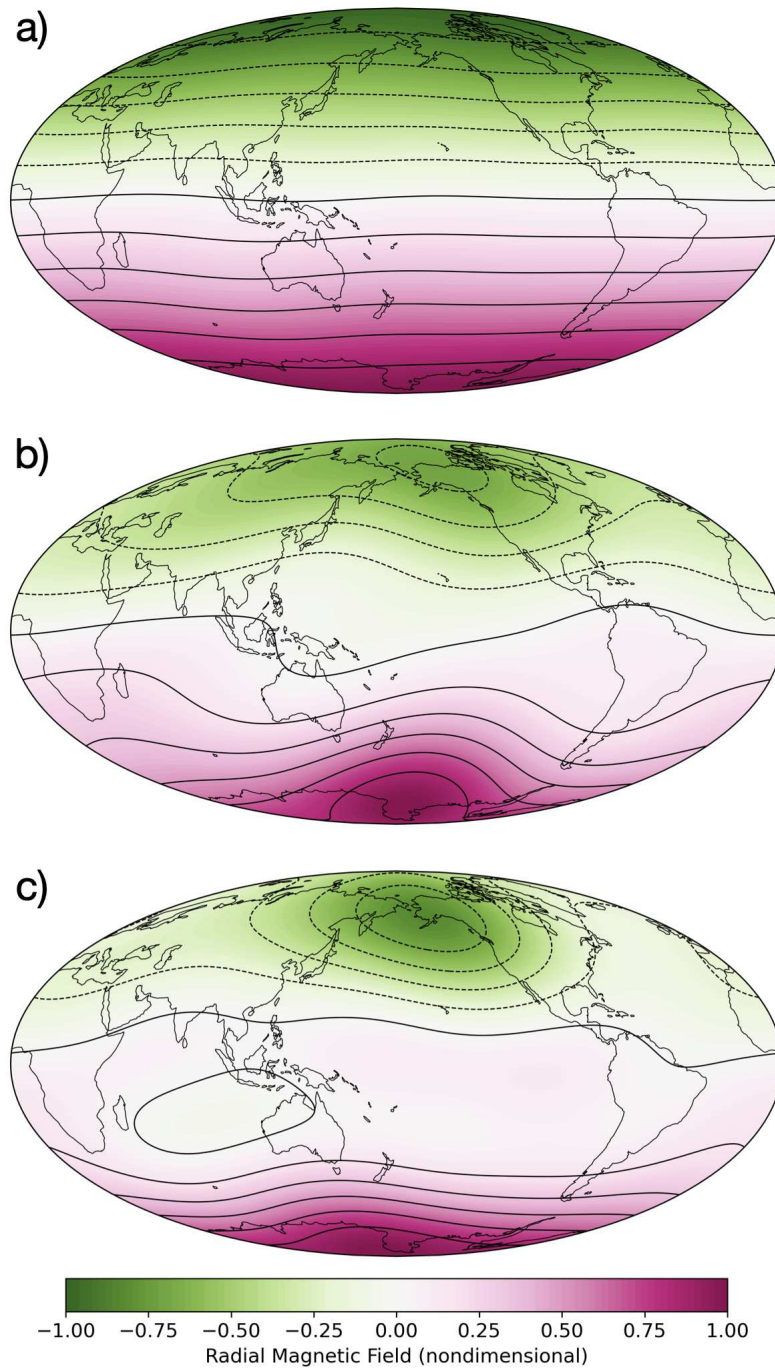


Figure 1: Time-averaged magnetic fields for our simulations with $Ra = 2000$ and $q^* = 0.0, 2.3, 5.0$ (a,b,c). The radial component of the magnetic field on the CMB truncated at spherical harmonic degree and order 4. All plots use the same colour scale.

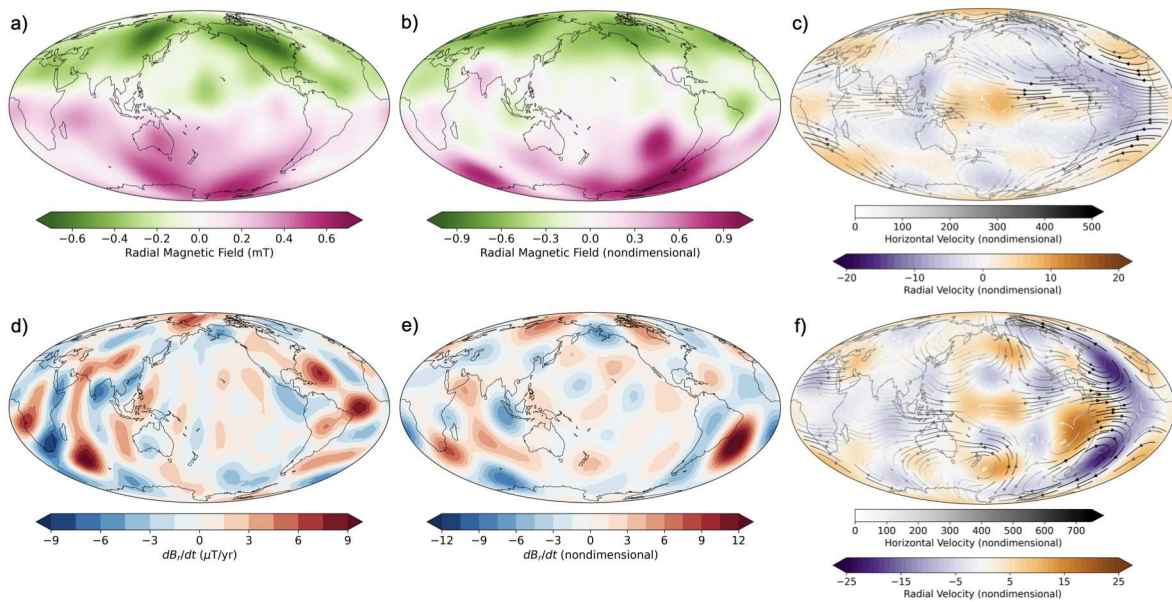


Figure 2: Comparison of our $Ra = 2000$ and $q^* = 2.3$ with *gufm1*. Time-averaged radial magnetic field at the core-mantle boundary from *gufm1* (a) and the best window of our simulation (b). Snapshot of secular variation in 1990 from *gufm1* (d) and the best window of our simulation (e). Time-averaged flow near the top of the core from the entire run of our simulation (c) and the best window (f). Magnetic and velocity fields are truncated at spherical harmonic degree and order 8.

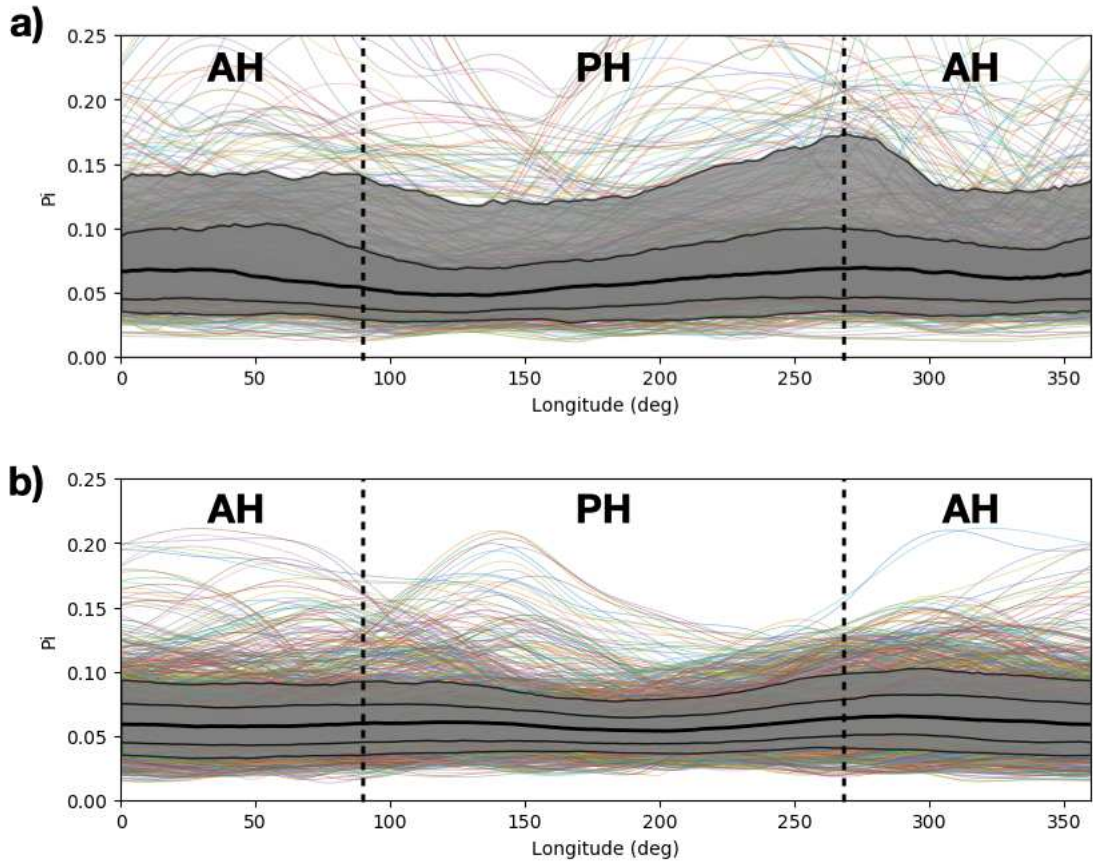


Figure 3: The longitudinal variation in paleosecular variation index (P_i) in the GGF100k observational model (a), and our $Ra = 2000$ and $q^* = 2.3$ simulation (b). Coloured lines are P_i calculated at individual time points, thick black line is the median, grey bands indicate the 10–90, and 25–75 percentiles. Vertical dashed lines designate the boundaries between the Pacific and Atlantic hemispheres.

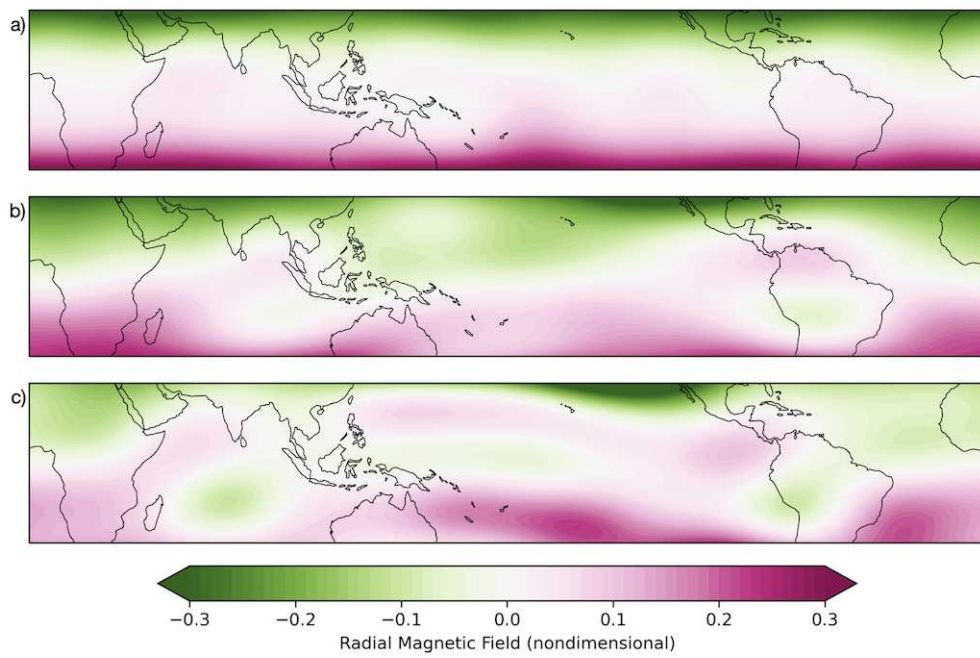


Figure 4: Time-averaged radial magnetic field at the core-mantle boundary in the equatorial regions of the simulations with $Ra = 2000$ and $q^* = 0, 2.3, 5$ (a,b,c). All plots use the same colour scale for the (non-dimensional) magnetic field strength and are truncated at spherical harmonic degree and order 8.

Supplementary Information for: Lower Mantle Heat Flow Controls the Longitudinal Structure of Earth's Magnetic Field

Jonathan E. Mound,^{1*} Christopher J. Davies,¹

¹School of Earth and Environment, University of Leeds, Leeds, UK, LS2 9JT

*To whom correspondence should be addressed; E-mail: j.e.mound@leeds.ac.uk.

Methods

Numerical Simulations

We numerically solve the magnetohydrodynamic equations for rotating convection in a spherical shell under the Boussinesq approximation. These equations include the conservation of momentum, energy, and mass, the magnetic induction equation, and an equation of state, with the influence of density variations ignored other than as a source of buoyancy. Nondimensionalisation of this system of equations suggests a set of control parameters for the simulations. The Ekman number, $E = \nu/2\Omega L^2$, describes the ratio of viscous to Coriolis forces (where, ν is kinematic viscosity of the fluid, Ω rotation rate, and L a characteristic length-scale, taken to be the thickness of the spherical shell). A Rayleigh number, $Ra = \alpha g_o \beta / 2\Omega \kappa$, describes the strength of buoyant driving relative to dissipation (where, α is the thermal expansivity of the fluid, g_o is gravitational acceleration on the outer boundary, κ is the thermal diffusivity of the fluid, and β is a measure of the average heat flux through the outer boundary). The Prandtl number, $Pr = \nu/\kappa$, and magnetic Prandtl number, $Pm = \nu/\eta$, relate the thermal, momentum, and magnetic diffusivities of the fluid (where, η is magnetic diffusivity). The simulations are

20 driven by thermal fixed-flux boundary conditions that are homogeneous on the ICB and hetero-
21 geneous on the CMB, with no internal heat source or sink. The amplitude of CMB heat flux
22 heterogeneity is described by $q^* = (q_{\max} - q_{\min})/q_{\text{ave}}$ (where, q_{\max} , q_{\min} , q_{ave} are the maximum,
23 minimum, and average values of CMB heat flux, respectively).

24 The amplitude of Earth's CMB heat flux variations is difficult to estimate because it must be
25 inferred from seismic tomography while accounting for the possibility of both thermal and com-
26 positional variations in the lower mantle. The nature of LLVPs is uncertain; however, the gen-
27 eral view is that these features are anomalously hot, even if they have a substantial compositional
28 contribution to their origin (1). Lateral variations in core-mantle heat flow due to the thermo-
29 chemical variations of the lowermost mantle have been estimated in studies combining insight
30 from seismic observations, mineral physics, and mantle convection simulations, which sug-
31 gested a minimum heat flux of $q_{\min} \approx 0 \text{ mW m}^{-2}$ and $q_{\max} \geq 200 \text{ mW m}^{-2}$ (2–4). The adiabatic
32 gradient at the top of the core is $\partial T_a/\partial r = g\gamma T/\phi \approx -0.875 \pm 0.125 \text{ K km}^{-1}$ with the seismic
33 parameter, ϕ , and gravity taken from PREM (5) and estimates for the Grüneisen parameter γ of
34 1.3–1.5 (6). Combined with the uncertainty in core thermal conductivity (7, 8), this gives a plau-
35 sible range of adiabatic heat flux at the top of the core of $q_a = -k\partial T_a/\partial r \approx 15 - 100 \text{ mW m}^{-2}$,
36 implying that hot LLVPs in the lower mantle will result in a subadiabatic heat flux across the
37 CMB. Overall, q^* of at least order 1 is expected and it could be larger than the values we con-
38 sider.

39 Solidification of the inner core releases light elements (9) that likely remain trapped within
40 the fluid core, providing an additional source of buoyancy at depth. If convection in Earth's core
41 is dominated by compositional buoyancy, then a homogeneous zero-flux condition for compo-
42 sition at the CMB might reduce the impact of thermal heterogeneity. Conversely, light elements
43 trapped in Earth's core might act to raise the effective value of q^* as, like heat conducted along
44 the adiabat, they represent a homogeneous source of buoyancy that is not available to promote

45 convection at the CMB. The overall impact of double-diffusive convection on Earth’s core dy-
 46 namics will depend on the balance of the thermal and compositional driving and their boundary
 47 conditions. An exploration of double-diffusive geodynamo conditions is beyond the scope of
 48 this work; however, previous work has found that a wide variety of such simulations can repro-
 49 duce Earth-like geomagnetic fields (10).

50 The dynamic conditions of Earth’s outer core are characterised by low Ekman, low Prandtl,
 51 and high Rayleigh numbers (11). Earth-like values of these parameters are not computation-
 52 ally accessible; however, we consider six simulations designed to have the appropriate bal-
 53 ance of forces. Our simulations are characterised by $E = 10^{-5}$, $Pr = 0.2$, $Pm = 1$,
 54 $Ra = \{2000, 6000\}$, and $q^* = \{0, 2.3, 5.0\}$ (Table 1). The pseudo-spectral method used in
 55 this work is described in more detail in (12). Velocity and magnetic field are decomposed
 56 into toroidal and poloidal scalars, so that the divergence-free conditions are exactly satisfied.
 57 All scalars are expanded in Schmidt-normalised spherical harmonics and represented in ra-
 58 dius by second-order finite differences. The finite difference points are located at the zeros of
 59 the Chebyshev polynomials, giving finer spacing near the boundaries of the fluid core. Time
 60 stepping is accomplished in spectral space using a predictor–corrector scheme that treats dif-
 61 fusion terms implicitly, while the Coriolis, buoyancy and nonlinear terms are treated explic-
 62 itly. Nonlinear terms are transformed into real space at each time step using the spherical
 63 transform method (13). At each radius multiplications are performed on a Gauss–Legendre
 64 grid with $(3/2)\ell_{\max}$ colatitude points and $3\ell_{\max}$ longitude points. For all simulations the num-
 65 ber of radial grid points, $N_r = 256$, and the maximum spherical harmonic degree and order,
 66 $\ell_{\max} = m_{\max} = 192$.

67 After removal of the initial transient, the resultant turbulent flows achieve an Earth-like
 68 (14, 15) magnetic Reynolds number (Rm of order 10^3), are strongly influenced by rotation
 69 (Rossby number, Ro , of order 10^{-2}), and generate relatively strong magnetic fields (as measured

70 by the Elsasser number, Λ). For the $Ra = 2000$ cases the average magnetic energy (ME) is a
71 few times greater than the average kinetic energy (KE), while for the $Ra = 6000$ cases they
72 are roughly equal for the heterogeneous boundary cases. These simulations are, therefore, in
73 the strong-field dynamo regime appropriate to Earth’s core (16). The $Ra = 6000$, $q^* = 0$
74 case is an unstable frequently reversing dynamo with a relatively weak magnetic field. We use
75 the magnetic diffusion time to re-scale the time and all cases have been run for a few tens of
76 thousands of years in order to obtain robust estimates of the time-averaged behaviour (17).

77 **Measures of Magnetic Field and SV Structure**

78 To compare geometric features of the radial CMB magnetic field between simulations and ob-
79 servational field models we compute the four compliance criteria of (18): the ratio of the power
80 of the axial dipole to the non-axial dipole field (AD/NAD); the ratio of power in odd versus
81 even spherical harmonic degrees (O/E); the ratio of zonal to non-zonal power (Z/NZ); and a
82 factor quantifying how strongly radial flux is concentrated into localised patches (FCF). Previ-
83 ous work (18) established a target value for each of these compliance criteria (C_i) by averaging
84 the over the 400-year long *gufm1* model (19) as well as an estimate of reasonable variability
85 (σ_i). For each characteristic the agreement of a simulation relative to the Earth is calculated as
86 $\chi_i^2 = \left[\left(\ln(C_i^{\text{sim}}) - \ln(C_i^{\text{gufm1}}) \right) / \ln(\sigma_i) \right]^2$. The total semblance ($\chi^2 = \sum \chi_i^2$) of a simulated
87 field compared to *gufm1* can then be classified as excellent ($\chi^2 \leq 2$), good ($2 < \chi^2 \leq 4$),
88 marginal ($4 < \chi^2 \leq 8$), or non-compliant ($8 < \chi^2$). The time-averaged value of the measures
89 and the total semblance for each run are reported in Tables 1 and 2.

90 The modern geomagnetic field has stronger secular variation (SV) in the Atlantic than in
91 the Pacific hemisphere (20, 21). We have previously constructed a measure of this hemispheric
92 imbalance (H_{sv}) and its variation which provides a χ^2 measure of compliance with respect
93 to the quiet Pacific secular variation (22). We determine the pattern of secular variation in

94 our simulations by calculating the centred differences of Gauss coefficients from successive
95 snapshots. We truncate the radial magnetic field at the CMB to spherical harmonic degree and
96 order 8 and average our simulations over consecutive 400-year windows to calculate statistics
97 of the compliance criteria throughout the runs.

98 The paleosecular variations index (P_i) developed in (23) is a non-dimensional measure that
99 can be constructed from observation of Earth's field at a given location and time. P_i depends
100 on the departure of the observed virtual geomagnetic dipole latitude (λ_p) from true north, and
101 on the departure of the observed virtual dipole moment (VDM) from the present-day value. For
102 example, if the VDM at a location is equal to the reference value of 80 ZAm^2 , then a doubling
103 of P_i from 0.05 to 0.10 corresponds to a change in λ_p from 81° to 72° . At each time point in
104 GGF100k and the simulations P_i is calculated on a two degree by two degree latitude-longitude
105 grid and these values are averaged over latitude to produce the longitudinal variation in P_i at
106 each point in time. The average character of P_i at a given longitude is taken to be the median
107 value from all time points, with the variability described by the 25-75 and 10-90 percentile
108 values.

109 Spatial variability in field activity is also shown in maps of the mean value of P_i over the
110 time span of each model (Supplemental Figure 4). The simulations allow for uniform high
111 spatio-temporal resolution; whereas, paleomagnetic data such as that used in GGF100k are
112 unevenly distributed in both space and time (24, 25). We compare to the observationally de-
113 rived spherical harmonic model rather than the data directly; so, we have not down-sampled
114 our simulation output to match the GGF100k sampling pattern. The simulations also provide
115 essentially instantaneous measurements of the magnetic field and its time derivative; whereas,
116 paleomagnetic records are variably smoothed in time depending on, for example, sedimenta-
117 tion rates during magnetisation acquisition, or the availability of tightly bound absolute age
118 constraints. Regional variation in this inherent temporal smoothing of the data (e.g., due to

119 different geological settings) could result in regional variation of P_i in a paleo-field model that
120 would be unrelated to the true variability of the geomagnetic field. Differences in the spatial and
121 temporal sampling of data must also be considered when comparing models such as GGF100k
122 with field models based on modern (observatory or satellite) observations. Despite extensive
123 computational effort, we are also only able to simulate a few combinations of mantle heat flux
124 heterogeneity and bulk core dynamics for the length of time required to obtain useful long-term
125 statistics. To help mitigate these considerations we mainly focus on the long wavelength and
126 time-averaged features of the simulated and observationally derived magnetic field models and
127 on features that are common across all of our $q^* \neq 0$ simulations.

128 **References**

- 129 1. A. K. McNamara, *Tectonophysics* **760**, 199 (2019).
- 130 2. T. Nakagawa, P. J. Tackley, *Earth and Planetary Science Letters* **271**, 348 (2008).
- 131 3. S. Stackhouse, L. Stixrude, B. B. Karki, *Earth and Planetary Science Letters* **427**, 11
132 (2015).
- 133 4. P. Olson, R. Deguen, M. L. Rudolph, S. Zhong, *Physics of the Earth and Planetary Interiors*
134 **243**, 44 (2015).
- 135 5. A. M. Dziewonski, D. L. Anderson, *Physics of the Earth and Planetary Interiors* **25**, 297
136 (1981).
- 137 6. H. Ichikawa, T. Tsuchiya, Y. Tange, *Journal of Geophysical Research* **119**, 240 (2014).
- 138 7. C. Davies, M. Pozzo, D. Gubbins, D. Alfè, *Nature Geoscience* **8**, 678 (2015).

- 139 8. Z. Konôpková, R. S. McWilliams, N. Gómez-Pérez, A. F. Goncharov, *Nature* **534**, 99
140 (2016).
- 141 9. K. Hirose, B. Wood, L. Vočadlo, *Nature Reviews Earth & Environment* **2**, 645 (2021).
- 142 10. T. Tassin, T. Gastine, A. Fournier, *Geophysical Journal International* **226**, 1897 (2021).
- 143 11. J. M. Aurnou, *et al.*, *Physics of the Earth and Planetary Interiors* **246**, 52 (2015).
- 144 12. A. P. Willis, B. Sreenivasan, D. Gubbins, *Physics of the Earth and Planetary Interiors* **165**,
145 83 (2007).
- 146 13. S. A. Orszag, *Studies in Applied Mathematics* **50**, 293 (1971).
- 147 14. N. Schaeffer, D. Jault, H. C. Nataf, A. Fournier, *Geophysical Journal International* **211**, 1
148 (2017).
- 149 15. M. Landeau, A. Fournier, H.-C. Nataf, D. Cébron, N. Schaeffer, *Nature Reviews Earth &*
150 *Environment* **3**, 255 (2022).
- 151 16. T. Schwaiger, T. Gastine, J. Aubert, *Geophysical Journal International* **219**, S101 (2019).
- 152 17. C. J. Davies, C. G. Constable, *Earth and Planetary Science Letters* **404**, 238 (2014).
- 153 18. U. R. Christensen, J. Aubert, G. Hulot, *Earth and Planetary Science Letters* **296**, 487
154 (2010).
- 155 19. A. Jackson, A. R. T. Jonkers, M. R. Walker, *Philosophical Transactions of the Royal Society*
156 *A: Mathematical, Physical and Engineering Sciences* **358**, 957 (2000).
- 157 20. R. Holme, N. Olsen, F. L. Bairstow, *Geophysical Journal International* **186**, 521 (2011).
- 158 21. C. C. Finlay, *et al.*, *Earth, Planets and Space* **72**, 156 (2020).

- 159 22. J. Mound, C. Davies, L. Silva, *Earth and Planetary Science Letters* **424**, 148 (2015).
- 160 23. S. Panovska, C. G. Constable, *Geochemistry Geophysics Geosystems* **67**, 83 (2017).
- 161 24. S. Panovska, C. G. Constable, M. Korte, *Geochemistry Geophysics Geosystems* **19**, 4757
162 (2018).
- 163 25. S. Panovska, M. Korte, C. G. Constable, *Reviews of Geophysics* **57**, 1289 (2019).

Additional Figures and Tables

Table 1: Dynamo Parameters that Vary Between Runs

Ra	q^*	Λ	Rm	Ro	ME/KE	Mean CC χ^2	Mean H_{SV} χ^2
2000	0.0	34	889	0.018	2.2	2.12	3.79
2000	2.3	39	851	0.017	2.7	5.39	4.24
2000	5.0	50	830	0.017	3.4	14.51	4.11
6000	0.0	26	1848	0.037	0.37	60.14	3.94
6000	2.3	43	1608	0.032	0.84	1.05	2.88
6000	5.0	62	1483	0.030	1.4	3.30	3.88

Table 2: Geomagnetic Field Measures

Ra	q^*	AD/NAD		O/E		Z/NZ		FCF		H_{sv}	
		mean	σ	mean	σ	mean	σ	mean	σ	mean	σ
<i>gufm1</i>	<i>gufm1</i>	1.4	2.0	1.0	2.0	0.15	2.5	1.5	1.5	-0.24	0.07
2000	0.0	1.27	0.28	1.88	0.50	0.21	0.13	2.38	0.87	0.03	0.12
2000	2.3	0.78	0.26	1.30	0.33	0.17	0.07	4.58	2.35	0.05	0.12
2000	5.0	0.41	0.10	1.01	0.21	0.23	0.11	9.57	3.70	0.05	0.11
6000	0.0	0.07	0.09	0.82	0.19	0.16	0.11	2.29	0.87	0.04	0.09
6000	2.3	1.23	0.26	1.47	0.34	0.26	0.08	1.54	0.34	-0.04	0.07
6000	5.0	0.92	0.23	1.56	0.42	0.26	0.09	3.10	1.60	0.03	0.04

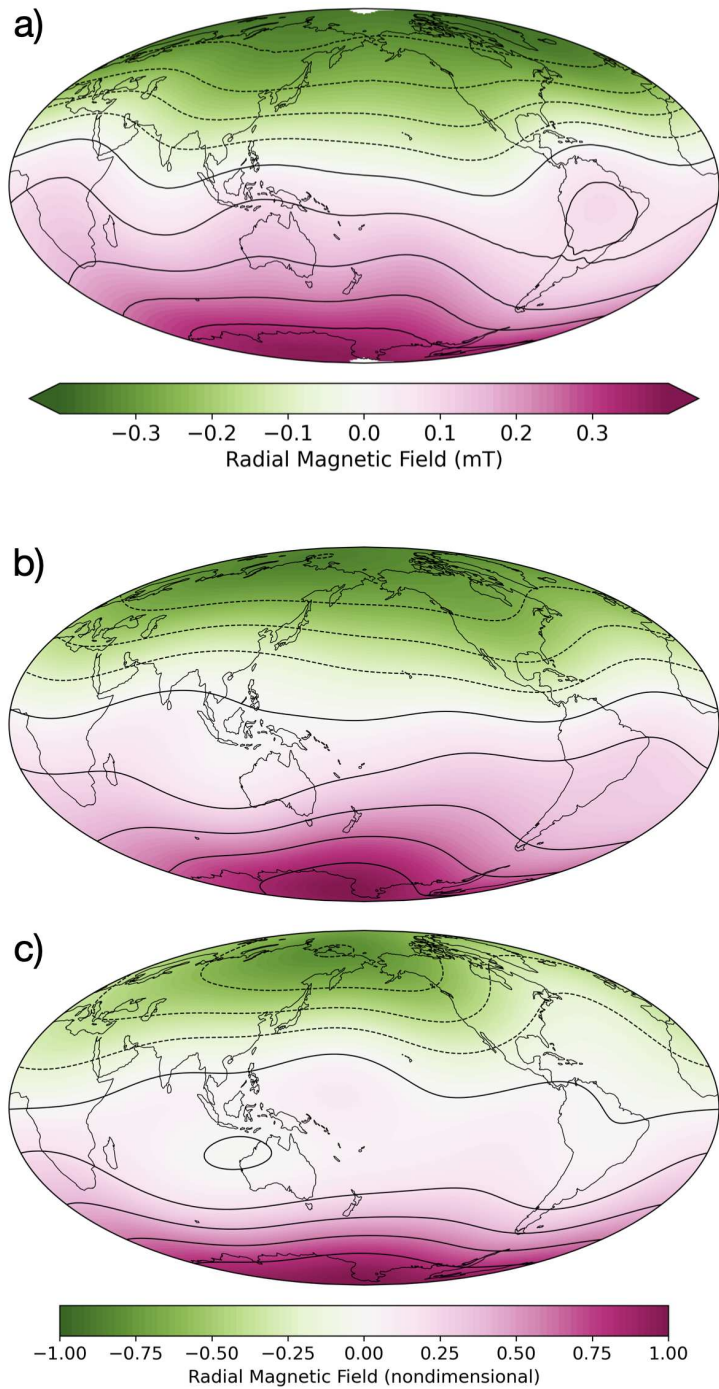


Figure 1: Time-averaged magnetic fields for GGF100k (a) and our simulations with $Ra = 6000$ and $q^* = 2.3, 5.0$ (b,c). The radial component of the magnetic field on the CMB truncated at spherical harmonic degree and order 4. Both simulation plots use the same colour scale.

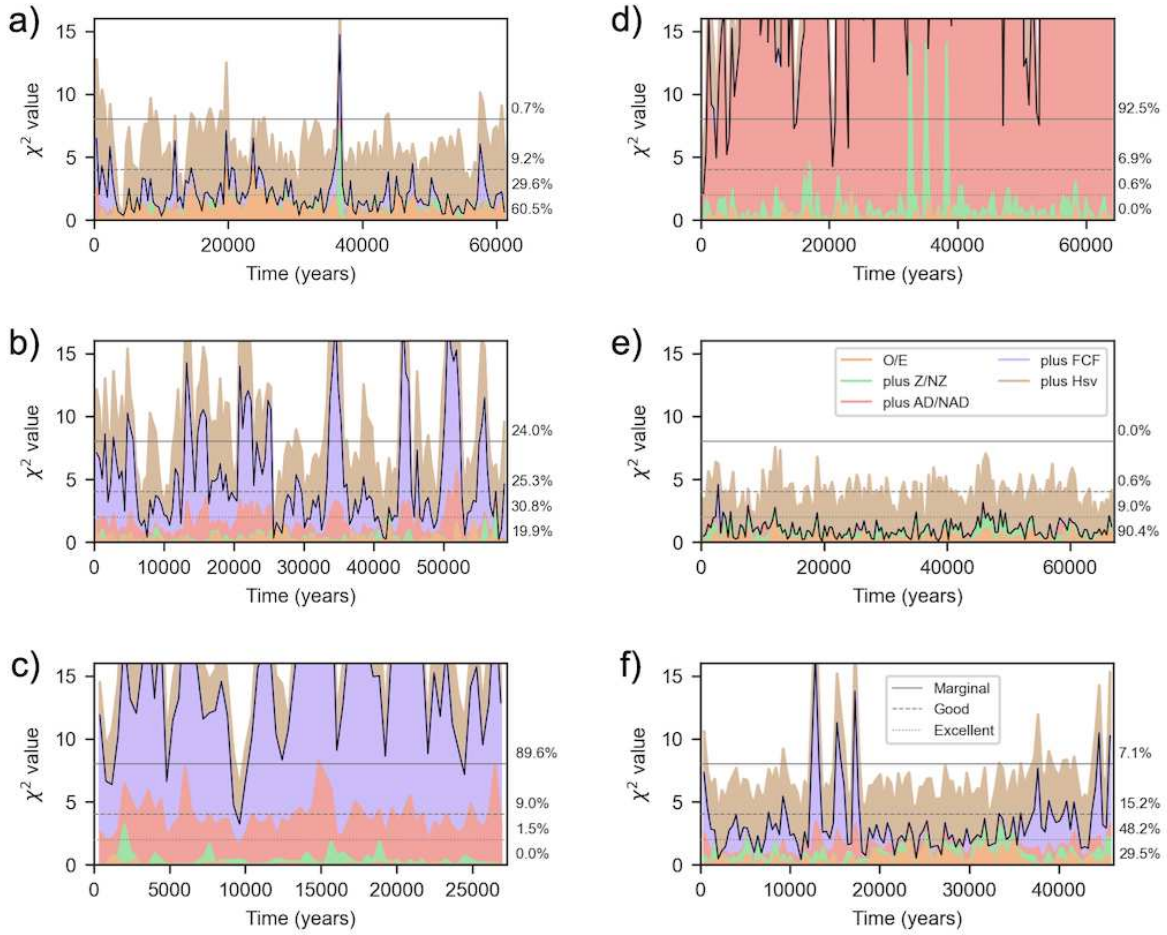


Figure 2: Evolution of the contributions to magnetic field and secular variation semblance over our simulations. The χ^2 contribution from the O/E, Z/NZ, AD/NAD, FCF, and H_{sv} measures are given by the orange, green, red, purple, and brown filled areas, respectively. The black solid line highlights the sum of the four compliance criteria for the magnetic field geometry and the grey horizontal lines indicate the values below which this total compliance is considered excellent, good, or marginal in comparison with Earth as derived from *gufm1*. Values to the right of each panel indicate the percentage of 400-year windows that fall in each compliance band. Simulations have $Ra = 2000$ (panels a,b,c) or $Ra = 6000$ (panels d,e,f) and $q^* = 0.0$ (a,d), $q^* = 2.3$ (b,e), or $q^* = 5.0$ (c,f).

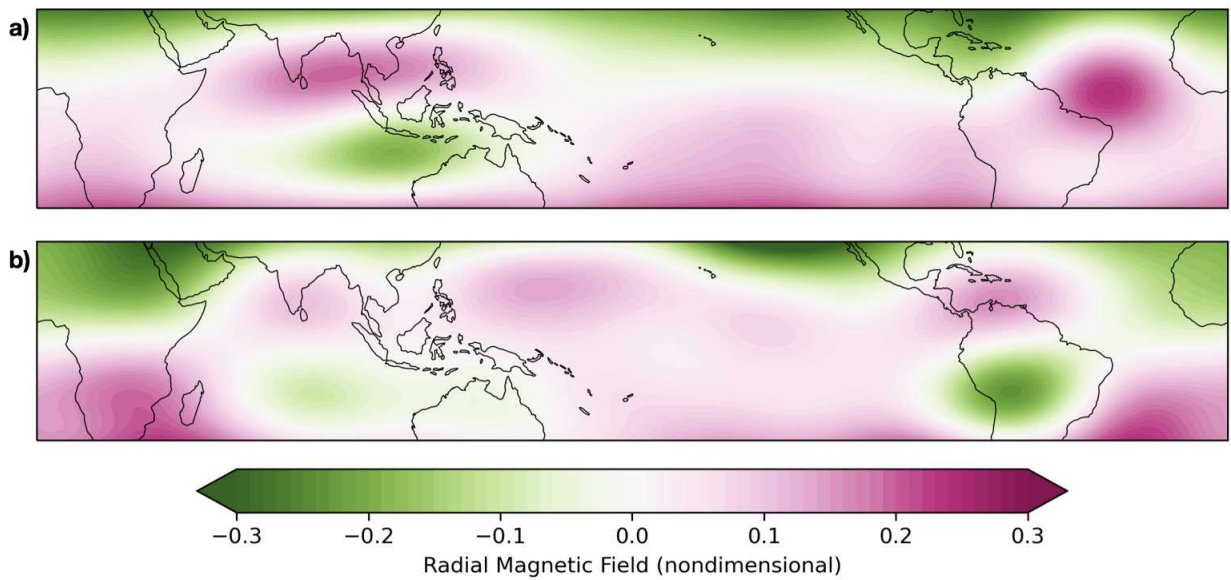


Figure 3: Time-averaged radial magnetic field at the core-mantle boundary in the equatorial regions of the simulations with $Ra = 6000$ and $q^* = 2.3, 5$ (a,b). Both plots use the same colour scale for the (non-dimensional) magnetic field strength and are truncated at spherical harmonic degree and order 8.

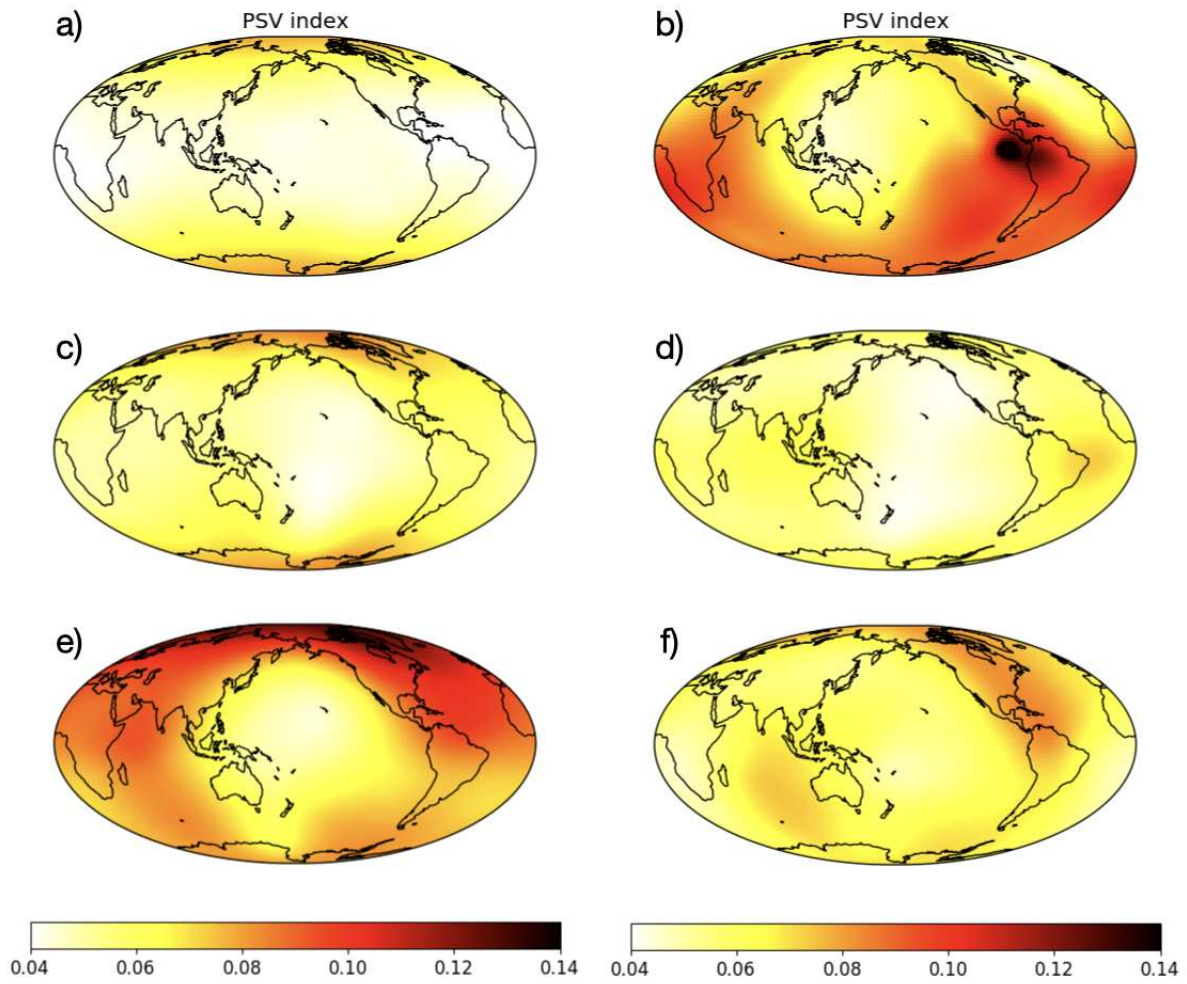


Figure 4: Time-averaged values of the paleosecular variation index from our simulations ($Ra = 2000$ and $q^* = 0, 2.3, 5$ (a,c,e); $Ra = 6000$ and $q^* = 2.3, 5$ (d,f) and GGF100k (b). All plots use the same colour scale.